Low-Complex Synchronization Method for Intra-Body Links in the Terahertz Band

Jorge Torres Gómez, *Senior Member, IEEE*, Jennifer Simonjan, *Member, IEEE*, and Falko Dressler, *Fellow, IEEE*

Abstract—Precision medicine applications supported by nanotechnologies enforce designing a communication interface between in-body nanosensors and external gateways. Such a communication interface will enable both a data and a control channel between nanodevices operating within the human body and external control units. In this direction, recent literature focuses on deriving analytic channel models for intra-body links through the human tissues, including the analysis of achievable communication capacities in the terahertz band. A yet missing component, however, is a synchronization module to implement communication schemes in the intra-body link. Such synchronization module will ultimately bound the communication performance regarding the perceived signal to noise ratio (SNR) and bit error rate (BER), for instance. This paper contributes to the state of the art in two directions: (a) evaluating the bounds on the communication performance with the Cramer-Rao lower bound (CRLB) for the synchronization symbol timing offset (STO) and (b) designing a low-complex mechanism to synchronize communication. This analysis considers a communication link between external gateways located on the skin and nanosensor devices flowing in the human vessels. Using envelope and slope detectors, we devise a low-complex solution that relies on the received signal strength (RSS) metric to trigger data emissions. The method estimates the peak of the received RSS metric to ignite communication in the most favorable location, i.e., when the nanosensor is located at the shortest distance in the communication range with external gateways. Our findings illustrate the feasibility of such a low-complex synchronization method. Performance illustrates a BER less than 1×10^{-5} for those nanosensors traveling close to the upper vessel wall.

Index Terms—Intra-body terahertz communication, Synchronization, Localization, In-body nanosensors

I. INTRODUCTION

ADVANCES in nanotechnologies progressively bridge the boundaries between the human body and the digital world. Battery-free electronics smoothly integrate with the skin as unnoticeable patches [1], integrating processing units running artificial intelligence (AI) modules, sensors [2], and radio frequency (RF) interfaces [3]. Inside the human body, nanotechnologies also allow radiating information from sensors to the outside through plasmonic antennas in the THz band [4]. Measurements with human-phantoms demonstrate the communication capabilities through the human tissues [5]. Such promising technologies advocate the paradigm of *cell-connected-to-internet*, where specific body regions are monitored and treated from remote locations, with impactful applications in precision medicine [6]. Making use of gateway systems, very powerful communication and control applications become possible [7], [8].

The THz band is becoming a promising means to convey information exchange in the nanoscale for precision medicine applications; see [9] for instance. Illustrative designs of RF components affords miniaturization in the μm size using graphene antennas [10], [11]. Numerous research advances the use of THz band communication, enabling communication among nanosensors in the human body and with external devices for monitoring and controlling applications [12].

Specifically, for intra-body links (inside to outside the body), recent studies on models render the propagation of THz waveforms, allowing us to evaluate the communication performance. These models compute the path loss when rays undergo through the tissue and define the noise produced by the surrounding molecules in the link [13]. Research also commends low-complex modulation schemes [14] like on-off keying (OOK) [4] and pulse position modulation (PPM) [15] to convey information between the nanonodes.

However, fulfilling the communication exchange in realistic scenarios requires implementing a synchronization scheme between emitter and receiver nodes [12], [16]. In the THz band, research reports timing acquisition algorithms detecting the average [17] and power levels [18] of received pulses, as well as using the maximum likelihood (ML) criterion with a training sequence [19]. Also, in the spectral domain, the phase of the incoming symbols is estimated using the Fourier transform as in [19]. Although these examples illustrate the feasibility of recovering the symbol timing in the THz band, these solutions are not applied to the particular case of intra-body channels. This requires a more thorough analysis and implementation when the communication happens through the human tissues.

Aiming to frame a communication interface in the THz band, we elaborate on a low-complex synchronization module to enable emissions between nanosensors traveling through the human vessels and external gateways attached to the skin's surface, as depicted in Fig. 1. Following our previous work in [20], nanosensors perform communication optimally (with the less bit error rate (BER)) when the packet is emitted along the channel coherence time and at the shortest distance in the communication range of the gateway. Consequently, the traveling nanosensor should synchronize emissions with their position relative to the gateway's location.

To implement such a synchronization mechanism, based on the spatial location of the nanosensor, we perform the periodic emission of pulses at the gateway and evaluate

Jorge Torres Gómez and Falko Dressler are with the School for Electrical Engineering and Computer Science, TU Berlin, Berlin, Germany, email: {torres-gomez, dressler}@ccs-labs.org.

Jennifer Simonjan is with Technology Innovation Institute, Masdar City, Abu Dhabi, UAE, e-mail: Jennifer.Simonjan@tii.ae.
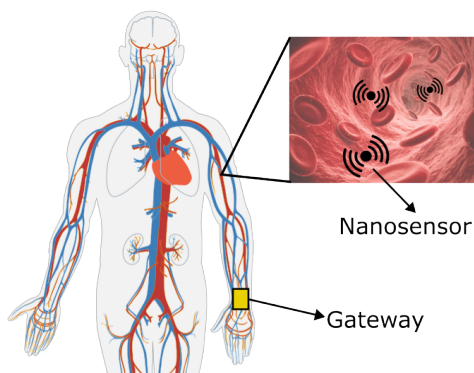
Fig. 1. Conceptual representation of nanosensors flowing through the HCS and a gateway attached to the hand of the person to collect the sensor data.

the backscattered received signal strength (RSS) from the nanosensor. The method, running at the more powerful gateway device, conceives a peak detector to evaluate the RSS's peak as an indicator of the shortest communication distance with the nanosensor. The RSS peak detection is used as a synchronization signal to trigger the data emission from nanosensors to the gateway.

Following the above, our key contributions can be summarized as follows:

- We design a low-complex synchronization method to trigger the communication in the intra-body link.
- We provide an analytic model describing the randomness of the RSS peak detection in the intra-body link.
- We evaluate the Cramer-Rao lower bound (CRLB) metric to evaluate the minimum variance of the RSS peak detection.
- We evaluate the performance for the proposed method with the symbol timing offset (STO) and the impact on the achievable BER.

Our findings illustrate the feasibility of devising a synchronization signal that triggers communication when the nanosensor travels near the vessel's upper wall.

Elaborating on these contributions, the rest of the paper is structured as follows. We discuss the state of the art in Section II. Details on the system model introducing the mobility of nanosensors and the communication channel model are given in Section III. In Section IV, we provide insights on the core idea to devise a synchronization signal with the RSS's peak and evaluate the minimum variance of such an estimation with the CRLB formulation. We detail the proposed low-complex mechanism in Section V with the corresponding block diagram and design parameters. Section VI illustrates the performance of the proposed design with the STO and the BER metrics. Finally, we summarize open research directions in Section VII and conclude the work in Section VIII

II. STATE OF THE ART

This section overviews the existing state-of-the-art in channel modeling and synchronization of THz channels. To the best of our knowledge, research is still lacking in the synchronization domain for in-body THz channels and there are no existing

works on synchronization of emissions with the position of the nanosensor. In this section, we therefore discuss relevant works focusing on developing clock recovery methods. Furthermore, we included comprehensive surveys on THz channel modeling and synchronization for further reading.

Gupta et al. [17] proposed a synchronization scheme for pulse-based THz-band communications, which aims at jointly determining the symbol start time and the observation window length. This is achieved by successively narrowing down the integration window to the true location of the pulse. Furthermore, the authors investigated the symbol error rate, the synchronization preamble length and the maximum number of bits to be transmitted before requiring re-synchronization analytically.

Han et al. [19] proposed two timing acquisition algorithms for pulse-based communications in the THz band. A low sampling rate (LSR) and maximum-likelihood (ML) algorithm are proposed for timing acquisition. They investigate the LSR algorithm by considering the antenna gain, the distance, the number of frames per symbol and the pulse width. However, the proposed LSR works only well if the SNR is significantly high. The ML approach instead adopts a two-step acquisition procedure to derive the timing acquisition solutions based on the ML criterion and works better in low SNR scenarios. Overall, the authors provide promising angles to efficiently and reliably solve the timing acquisition problem for pulse-based THz band wireless systems. Furthermore, this work provides a comprehensive overview of existing synchronization approaches.

A link-layer synchronization and medium access control (MAC) protocol for very-high-speed wireless communication networks in the THz band has been presented by Xia et al. [21]. The proposed protocol relies on a receiver-initiated handshake as well as a sliding window flow control mechanism to guarantee synchronization between transmitter and receiver, maximize the channel utilization and minimize the packet discard probability.

A novel receiver architecture for pulse-based electromagnetic nanonetworks in the Terahertz band has been proposed by Cid-Fuentes et al. [18]. The proposed architecture is based on a Continuous-time Moving Average (CTMA) symbol detection scheme and bases its symbol decision on the received signal power maximum peak after the CTMA, which is implemented with a single low-pass filter.

Furthermore, there are some recent interesting and comprehensive surveys discussing THz technologies, channel models, modulation schemes, topologies, synchronization and localization techniques, which we would like to refer the reader to. For example, Saeed et al. [22] presented a study of the THz band for body-centric networks, by surveying works on THz device technologies, channel and noise modeling, modulation schemes, and networking topologies.

Another relevant survey has been published by Lemic et al. [12], who have provided an overview of the current status in THz nano-communication and nano-networking research. Specifically, the authors introduce existing works regarding network, link and physical layer protocols as well as THz channel models.

Chen et al. [23] presented an extensive overview of existing THz systems and localization surveys. Even if the study focuses on macro-scale setups rather than on the in-body scenario, it includes important discussions about THz channels and points to further surveys and works dealing with localization. Finally, Akyildiz et al. [16] reviewed the recent advancements and highlighted the open research directions of THz communications thoroughly, discussing also synchronization and localization specifics of the THz band.

In these reported works, a synchronization module for intra-body links is still missing. To design such a module, we rely on our prior work [20], which studies the intra-body communication channel between nanosensors in the bloodstream and gateways attached to the skin using the THz spectrum. In [20], we focused on developing a communication scheme that considers the waveform to be travelling through three layers of skin, tissue, and blood. The main conclusion of this work was that optimal communication happens when the nanosensor is below the gateway. This requires the development of a module to synchronize emissions with the nanosensor's location. Contributing to that direction, this work now focuses on developing and analyzing the performance of a low-complex mechanism to ignite communications between nanosensors and the gateway.

III. SYSTEM MODEL

As for the system model, we consider the intra-body communication link between nanosensors traveling through the human vessels and an external gateway located on the skin's surface. This system is sketched in Fig. 2, illustrating the local communication scenario between the nanosensor and the gateway. The reference coordinates are centered horizontally with the gateway location and in the ordinate with the upper vessel wall, where the l_v-coordinate defines the vessel stream. The nanosensor passively moves straight from left to right along the vessel stream, driven by the blood flow and at a constant speed v_{l_v}, which defines the nanosensor position along the x-axis as $x = v_{l_v} t$. [1]

Besides, we implicitly assume that advection dominates diffusion as the nanosensor displaces along the same vessel stream (l_v) in the communication range with the gateway. This condition will be valid whenever $v_{l_v} \gg \frac{D}{L_{\text{comm}}}$, where D is the nanosensor's diffusion coefficient,[2] and L_{comm} is the communication range along the blood flow, see [25, Eq. (19)].

The nanosensor and the gateway communicate along three layers through the blood vessels, the fat tissue, and the skin. Communication occurs in the THz band 0.1 to 10 THz [13]. We perform emissions at the center frequency of $f_c = 0.14$ THz, with the communication bandwidth BW = 40 MHz, and with isotropic antennas. We assume that the communication distance is at most $d_{\text{max}} = 1.5$ mm to avoid that much attenuation level [26].[3] Further details on
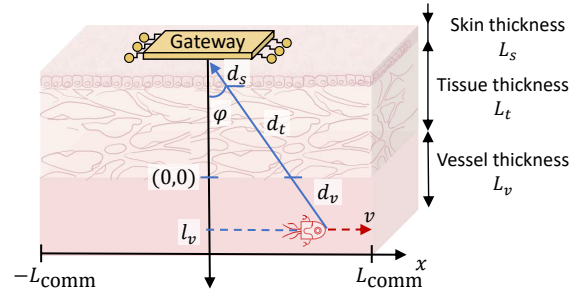

Fig. 2. System model for the communication system between the nanosensor and the gateway.

these physiological parameters are given in Table I and the corresponding references [27]–[29]. As a result, the communication range $[-L_{\text{comm}}(l_v), L_{\text{comm}}(l_v)]$ in the direction of mobility, see Fig. 2, will be determined by

$$L_{\text{comm}}(l_v) = \sqrt{d_{\text{max}}^2 - (L_v + L_t + l_v)^2}, \qquad (1)$$

which is dependent on the nanosensor's vessel stream l_v.

The received signal at the gateway is modeled with the channel path loss and including the impact of additive white gaussian noise (AWGN) as[4]

$$r(t) = \sqrt{\frac{P_{\text{Att}}}{2} P_{\text{Tx}}} s(t) + w(t), \qquad (2)$$

where $s(t)$ is the emitted sequence, P_{Att} is the power attenuation introduced by the channel in one direction only, and P_{Tx} is the transmission's power. We include the $\frac{1}{2}$ factor as we consider the backscatter signal, i.e., the signal travels from the gateway to the nanosensor and is backscattered to the gateway by the nanosensor. Consequently, the received signal will be a Gaussian variable following the distribution

$$r(t) \sim \mathcal{N} \left(\sqrt{\frac{P_{\text{Att}}}{2} P_{\text{Tx}}} s(t), \sigma^2 \right), \qquad (3)$$

where σ^2 is the noise power.

We assume the noise level produced by the human tissue (molecular absorption noise) is negligible compared to the noise produced by the receptor circuit. To illustrate this concern, the noise produced by the human tissue will be less than the amount $k_B T_{\text{mol}} \text{BW}$, where k_B is the Boltzmann constant, $T_{\text{mol}} = T_0(1 - e^{-4\pi f_c(L_v+L_t+L_s)k/c})$, $T_0 = 310$ K is the reference temperature, $k = 0.0072$ is the extinction coefficient, and BW is the communication bandwidth. Evaluating the minimum bandwidth (BW), as two times the sampling time, yields BW $= \frac{2}{T_s} = 40$ MHz, as for T_s we follow the value listed in Table I. To illustrate, with this formulation the power of the molecular absorption noise results in ~ -140 dB.

On the other hand, the noise level in the receptor circuit is evaluated with the noise equivalent power metric, which is reported as $1 \text{ nW/Hz}^{1/2}$ at 0.04 and 0.14 THz [30]. Assuming the same communication bandwidth (BW = 40 MHz),

---

[1] Implicitly, here we assume that $t = 0$ corresponds to the nanosensor's position just below the gateway.

[2] The nanosensor's diffusion coefficients will be directly related its size and shape, see examples in [24, Fig. 4.5 pag. 57]

[3] Distances less than 2 mm happen between on the wrist between the skin surface and the capillaries, for instance.

[4] Following our previous work in [20] we assume transmissions are performed along the channel coherence time, thereby avoiding the impact of mobility with the Doppler effect.

the resulting noise level by the circuit is evaluated as $1\,\text{nW/Hz}^{1/2} \times \sqrt{\text{BW}}$, yielding $\sim -62\,\text{dB}$. This value is comparatively larger than the noise level in the human tissue ($\sim -140\,\text{dB}$), allowing us to disregard the molecular absorption noise.

In Eq. (3), the attenuation power in the human tissues follows the predefined equations in [26, Eq. (2)], accounting for the spreading and molecular absorption losses, as

$$P_{\text{Att}} = e^{-\mu_v d_v} \times \left(\frac{\lambda_v}{4\pi d_v}\right)^2 \times e^{-\mu_t d_t} \times \left(\frac{\lambda_t}{4\pi d_t}\right)^2 \times e^{-\mu_s d_s} \times \left(\frac{\lambda_s}{4\pi d_s}\right)^2, \tag{4}$$

including the attenuation in the three layers (vessel, tissue, and skin), where μ_v, μ_t, μ_s are the molecular absorption coefficients, and λ_v, λ_t, and λ_s are the effective wavelengths of the vessel, tissue, and skin, respectively.[5] The variables d_v, d_t, and d_s account for the communication distance between the nanosensor and the gateway in the vessel, tissue, and skin, respectively, see their representation in Fig. 2.

These communication distances can be evaluated with the time-varying position of the nanosensor along the x-axis as given by $x = v_{l_v} t$. Using the cosine function for the incidence angle of the communication signal ray (φ in Fig. 2), straightforward calculations evaluate d_v, d_t, and d_s as

$$d_v = \frac{l_v}{\cos\varphi}, \quad d_t = \frac{L_t}{\cos\varphi}, \text{ and } \quad d_s = \frac{L_s}{\cos\varphi}, \tag{5}$$

$$\text{with} \quad \cos\varphi = \sqrt{1 - \left(\frac{v_{l_v} t}{l_v + L_t + L_s}\right)^2},$$

which is ultimately parametrized with time (t) and the vessel stream (l_v). The term v_{l_v} evaluates the speed with the vessel stream, which follows a parabolic profile as in [24, Eq. (4.9) pag. 54]

$$v_{l_v} = \frac{4v_m}{L_v^2}(L_v l_v - l_v^2), \tag{6}$$

where v_m denotes the maximum speed as in the vessel center. Finally, considering all the above expressions in Equations (5) and (6), we remark that the path loss in Eq. (4) will ultimately be a time varying function and dependent on the vessel stream the nanosensor travels with the variable l_v.

IV. IDENTIFICATION OF OPTIMAL POSITION FOR COMMUNICATION

As we discussed in our previous work in [20], the optimum communication performance occurs when the nanosensor is located just below the gateway, and all data is sent along the channel coherence time. This results from balancing the impact of the nanosensor's mobility and noise. Fig. 3 depicts the achieved BER and the total of information blocks with the transmission bandwidth as derived in [20], where each block refers to a bit sequence emitted along the channel coherence

[5]The molecular absorption coefficients and the effective wavelengths are evaluated as indicated in [26, Eq. (3)] and using the parameters in Table I in the same reference. Besides, although not directly stated here, P_{Att} in Eq. (4) is also frequency dependent with the effective wavelength parameters.
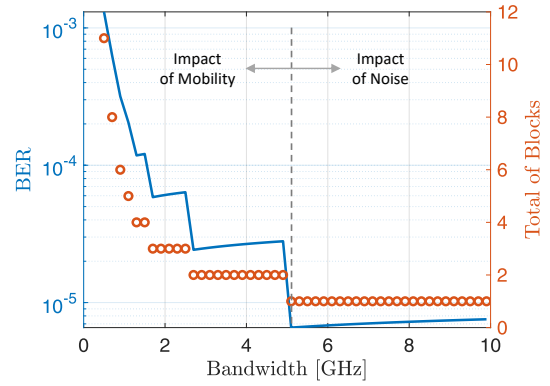

Fig. 3. Resulting BER and total of emission blocks, see [20].

time. In this plot, the nanosensor always emits the first block just below the gateway, and the remaining ones at shifted nanosensor's positions, as driven by the blood flow. Less transmission bandwidth implies emitting more than one block, which implies a degraded BER.

On the other hand, increased transmission bandwidth will increase the impact of noise and eventually degrade the BER. Consequently, the optimum communication performance is "spatially located" where the communication distance is minimum, i.e., at $\varphi = 0$ in Fig. 2. Besides, this optimal transmission strategy occurs with less possible transmission bandwidth that allows emissions to be performed within a single communication block.

Following this rationale, a strategy to optimize the communication performance is to estimate the distance between the traveling nanosensor and the gateway. Then, synchronously ignite the data emission when this distance is the minimum along the nanosensor's path. The literature reports two primary metrics to estimate the distance with the received signal: the RSS and the time of flight (ToF). To conceive the less complex scheme, we analyze the RSS metric and let for future work the ToF and the combination of both.

With the RSS metric, the minimum distance can be detected with the maximum power of the received signal evaluated as

$$P_{\text{Rx}} = \frac{1}{2}P_{\text{Att}}(t; l_v)P_{\text{Tx}}. \tag{7}$$

To illustrate, Fig. 4 provides a view of the RSS metric with the nanosensor's position in (a) and with time in (b). These plots are derived with the electric and physiological parameters in Table I, and using [26, Table. I] for the absorption coefficients in the human tissues. These plots directly evaluate Eq. (7) for various traveling paths across the vessel streams (l_v).

As expected, all the peaks occur at $x = 0$ where the gateway is located, see Fig. 4a). However, depending on the nanosensor's vessel stream, the peak is observed earlier or later with time, see Fig. 4b). The peak appears earliest when l_v approaches the vessel center, where the blood speed is the fastest, and it delays with the decreasing distance to the vessel edges, where the blood speed approaches zero. Specifically, the time instant

for the RSS' peaks can be readily evaluated as

$$t_{\text{peak}} = \frac{L_{\text{comm}}(l_v)}{v_{l_v}}, \tag{8}$$

as the nanosensor displaces with constant speed along the vessel stream with $L_{\text{comm}}(l_v)$ as given in Eq. (1). Estimating the peak location with t_{peak} in Eq. (8) will readily provide the synchronization signal needed to ignite the optimum communication performance.

However, estimating the peak location will inherently encompass an error, which is lower bounded by the variance produced by the noise component. The location and amplitude of the RSS's peak will be a random variable that depends on the random vessel stream the nanosensor travels and the noise that is part of the communication channel. The parameter l_v is a random variable of arbitrary distribution, and the amplitude of the received signal is also impacted with the AWGN random noise $w(t)$ as in Eq. (2). In the next Sections, we derive such a variance with the CRLB metric and illustrate the boundaries on the communication performance for reported electronic noise-powers.

A. Minimum STO to estimate the RSS peak location

We evaluate the minimum error for the RSS peak detection with the STO metric. The STO refers to the time difference between the detected symbol and the actual arrival time instants [32]. This metric evaluates the accuracy of synchronizers and ascertains communication metrics like the signal to noise ratio (SNR) and the BER.

As the RSS peak's location is a random variable, the STO will be lower bounded with half of the standard deviation of t_{peak}, yielding

$$\text{STO}_{\min} = \frac{1}{2}\sqrt{\text{var}(\hat{t}_{\text{peak}})}, \tag{9}$$

To evaluate $\text{var}(\hat{t}_{\text{peak}})$ in Eq. (9), we resort to the CRLB metric, as it assesses the lower bound for unbiased estimators [33, Chap. 3]. As t_{peak} depends on the vessel stream

TABLE I
SIMULATION PARAMETERS

Parameter	Variable	Value	Reference
Pulse shape	Rectangular pulse		
Pulse duration	T	1 µs	
Pulse period	T_p	1 ms	
Receiver's sensitivity		0.1 nW/Hz$^{1/2}$	[30]
Center Frequency	f_c	0.14 THz	[30]
Sampling time	T_s	50 ns	
Blood speed in the veins	v	0.03 m/s	[31]
Skin thickness	L_{skin}	76 µm	[27]
Tissue thickness	L_{tissue}	1 mm	[28]
Vessel thickness	L_{vessel}	200 µm	[29]
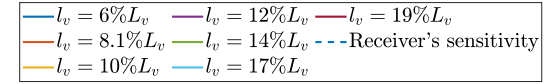
(a) Received power with the x-coordinate
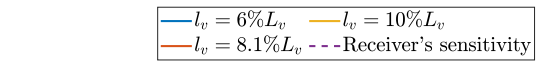
(b) Received power with time

Fig. 4. Received power at the gateway with the nanosensor's position along the x-direction and with time.

parameter l_v (see Eq. (8)), we formulate the CRLB for t_{peak} in terms of the CRLB for l_v as [33, Eq. (3.16) pag. 37]

$$\text{var}(\hat{t}_{\text{peak}}) \geq \text{CRLB}_{t_{\text{peak}}} \tag{10}$$
$$= \left(\frac{\partial t_{\text{peak}}}{\partial l_v}\right)^2 \text{CRLB}_{l_v}\big|_{l_v = l_v^{-1}(t_{\text{peak}})},$$

allowing us to focus on evaluating the lower bound for the l_v parameter estimation instead. In this equation, the partial derivative is solved directly by derivating Eq. (8) after replacing its numerator with Eq. (1) and its denominator with Eq. (6).

The term CRLB_{l_v} in Eq. (10) refers to evaluating the minimum variance to estimate the vessel stream l_v based on the received amplitude. Its calculation becomes straightforward due to the dependence of the amplitude sequence with the vessel stream, as follows from Equations (4), (5) and (7). To evaluate this term, the amplitude of the received signal ($\sqrt{\frac{P_{\text{Att}}}{2}}P_{\text{Tx}}$ in Eq. (2)) is conveniently isolated when sampling $r(t)$ with the emitted pulse period (T_p),[6] and assuming the pulse's amplitude

[6]Without restraining the theoretical calculations for the minimum variance of the peak location, we assume such an ideal sampling process with the pulse period.

as one. Sampling Eq. (2) with T_p, the resulting sequence will follow the received amplitude level as follows

$$r[n] = A[n; l_v] + w[n], \tag{11}$$

where

$$A[n; l_v] = \sqrt{\frac{P_{\text{Att}}(nT_p; l_v)}{2} P_{\text{Tx}}}. \tag{12}$$

Eq. (11) yields a constant $A[n; l_v]$ embedded in a white Gaussian noise variable $w[n]$, as $w[n]$ is the sampling of the white Gaussian variable $w(t)$ in Eq. (3). Finally, due to Gaussian distribution for $A[n; l_v]$, we use [33, Eq. (3.14) pag. 36] to evaluate the CRLB_{l_v} term as follows

$$\text{CRLB}_{l_v} = \frac{\sigma^2}{\sum_{n=0}^{N_{l_v}} \left(\frac{\partial A[n; l_v]}{\partial l_v} \right)^2}, \tag{13}$$

where N_{l_v} denotes the total of samples in the time window where the received amplitude is above the receptors' sensitivity level. As illustrated in Fig. 4 b), this time window will depend on the vessel stream l_v as it decreases with l_v approaching the vessel center.

Following this development, we provide a straightforward calculation path for the STO_{min}. After calculating the partial derivative in Eq. (10), and evaluating the CRLB_{l_v} with Eq. (13), we can readily compute the right term in Eq. (10). The next Section illustrates its calculation with the parameters provided in Table I.

B. Evaluating the CRLB and the resulting SNR

To illustrate, Fig. 5 depicts the evaluation of Eq. (9) with the vessel stream.[7] This plot is derived using the communication and vessels parameters listed in Table I, as well as electric parameters in the human body from [26, Table I]. We evaluate the noise power as explained in Section III yielding $\sigma^2 = --62\,\text{dB}$. According to this plot, the STO_{min} results in the order of the ms. Such an STO amount can be only produced when the nanosensor travels quite close to the vessel walls (in this plot depicted in the range 6 to 10 % of the vessel thickness); rapidly increasing to the units of seconds for larger l_v's.

As a result of the non-zero STO in this range, the communication performance degrades. To illustrate, Fig. 6 depicts the resulting SNR with the vessel's stream and in comparison to the case of an ideal receiver, where the STO is zero. To obtain this curve, the SNR is evaluated as

$$\text{SNR}_\text{d} = \frac{P_{\text{Rx}}(t_{\text{peak}} + \text{STO}; l_v)}{\sigma^2}, \tag{14}$$

As Fig. 6 depicts, the received power becomes comparable to the noise level when the vessel stream becomes larger than 7 %, as a result of $\text{SNR} \approx 0$. The impact of the STO rapidly increases the gap with the ideal receiver.

These theoretical results indicate the need to conceive a synchronization scheme and delimit practical distance limits where intra-body communication can occur. The following
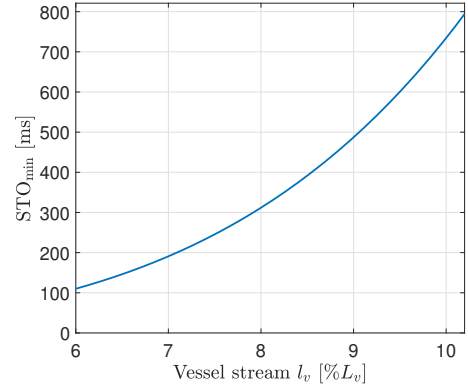

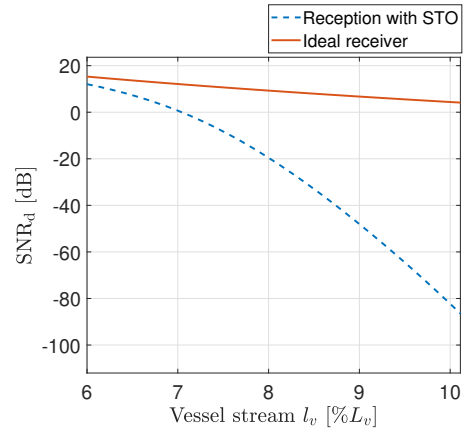Fig. 5. Minimum STO with the vessel stream l_v when the noise power is $\sigma^2 = -62\,\text{dB}$.

Fig. 6. Perceived SNR with the vessel stream l_v when the noise power is $\sigma^2 = -62\,\text{dB}$.

Section introduces a low-complex synchronization scheme to illustrate a method that can be implemented in practice. Based on this proposal, we later evaluate its limits on the achievable communication distance with the BER, as introduced in the Results Section.

V. SYNCHRONIZATION METHOD

We realize the synchronization method at the gateway due to its more extensive computational capabilities than the nanosensor. The gateway emits a pulse train sequence that travels into the tissue and measures the RSS metric for the bounced signal. The synchronization signal will be generated at the gateway with the detection of the RSS's peak.

Fig. 7 depicts the synchronization scheme implemented at the gateway. The gateway emits a pulse train to the tissue; see Fig. 7 a) and b), and will receive the bounced signal from the nanosensor.[8] The received sequence is an amplitude time variable pulse train as in Fig. 7 c), where the peak amplitude (represented as t_{below}) is aligned with the shortest distance between the nanosensor and the gateway, i.e., when the nanosensor's position is below the gateway.

---

[7]The code to evaluate the CRLB is publicly accessible at https://github.com/jorge-torresgomez/Terahertz_C_Matlab_codes

[8]In this scheme, we omitted to represent the upconversion and downconversion steps. Implicitly, we assume both operations are compensating to each others.
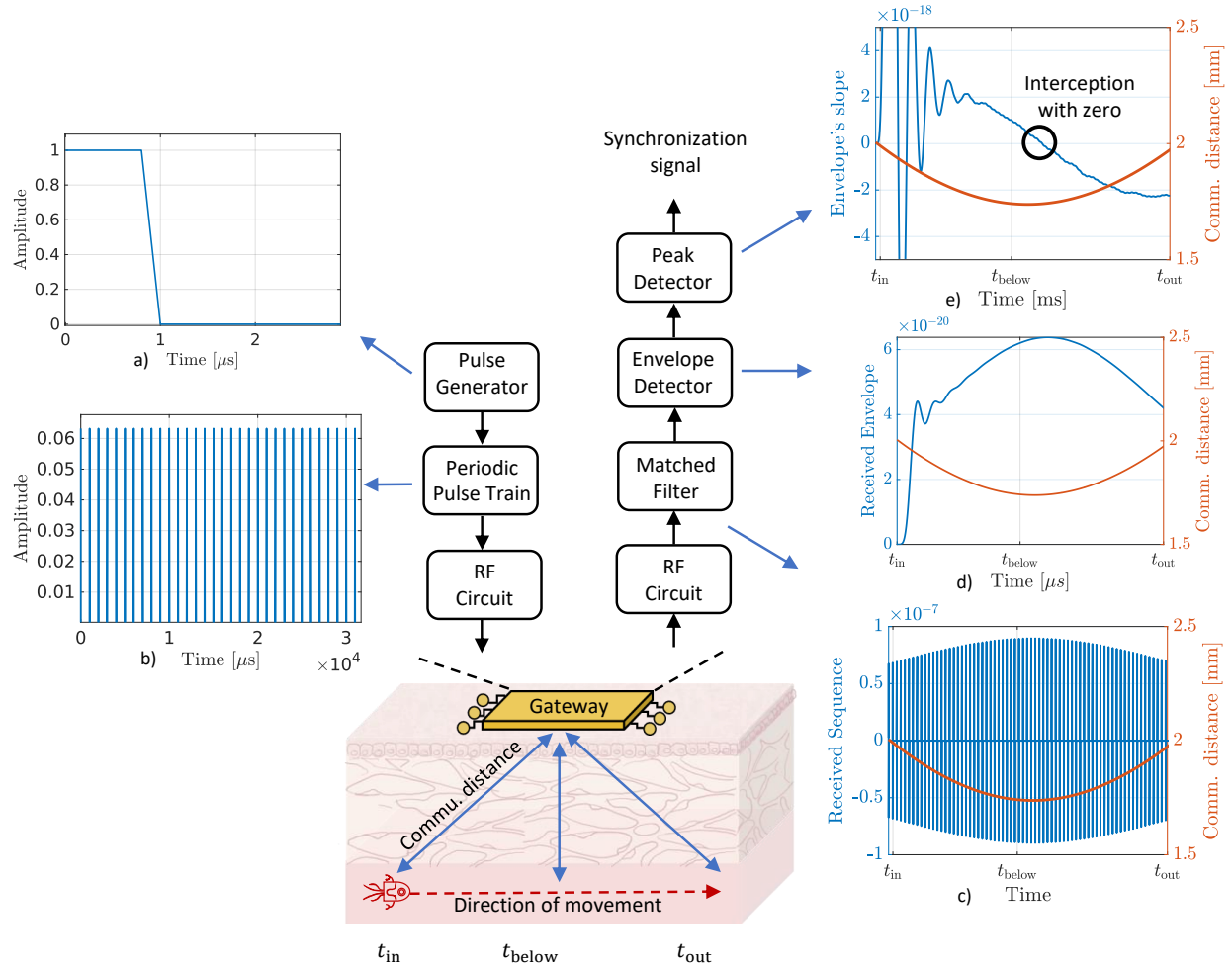
Fig. 7. Reference coordinate system for a nanosensor flowing through a blood vessel and communicating to a gateway outside the body.

The gateway detects the incoming sequence with a matched filter to maximize the detection performance [34]. The matched filter is implemented with a finite impulse response (FIR) filter, where the coefficients are the samples of the emitted rectangular pulse after normalizing it with the square root of its average power. Then, the gateway recovers the envelope at the output of the matched filter block exhibiting a peak close to t_{below}, as sketches Fig. 7 d). Finally, a peak detector module will locate the envelope's peak with the zero crossing time of the slope, as represented in Fig. 7 e). The gateway will produce the synchronization signal by detecting the zero crossing of the differentiator's output.

A. Envelope Detector Scheme

We implement the envelope detector using a low complex lowpass filter scheme, see [35, Sec. 4.5 pag. 176]. We take the squared value (instantaneous power) of the matched-filter output block, and lowpass filter it to follow the amplitude variations only; see the scheme in Fig. 8. The lowpass operation is implemented with an infinite impulse response (IIR) filter to reduce the number of coefficients when compared to the counterpart alternative FIR filter. Specifically, we implement a Butterworth lowpass filter due to its maximally flat bandpass
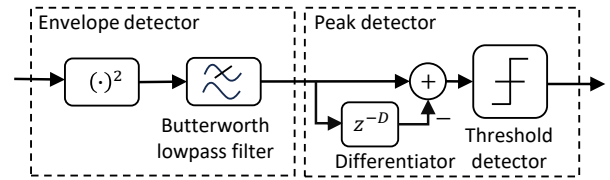

Fig. 8. Synchronization scheme.

magnitude, introducing the least amplitude distortion on the recovered envelope; see [36, Appendix B.1].

We implement a 12th-order Butterworth filter in the discrete domain with the 3 dB cutoff frequency at half the pulse train periodicity ($f_c = \frac{1}{2T_p}$), with $T_p = 1\,\text{ms}$ according to the parameters in Table I.[9] Fig. 9 depicts the filter's magnitude and group delay response. As expected, the magnitude results flat in the bandpass, and the non-zero group delay introduces a time shift in the peak amplitude of less than 5 ms. This time shift will introduce additional STO due to the digital signal processing (DSP) operation.

[9]See details on Butterworth filter design in [36, Sec. 7.1 pag. 442]
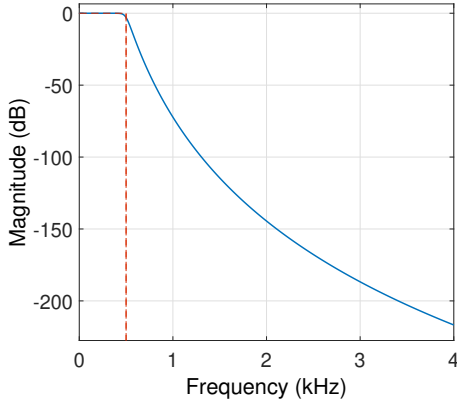
(a) Magnitude response for the Butterworth filter
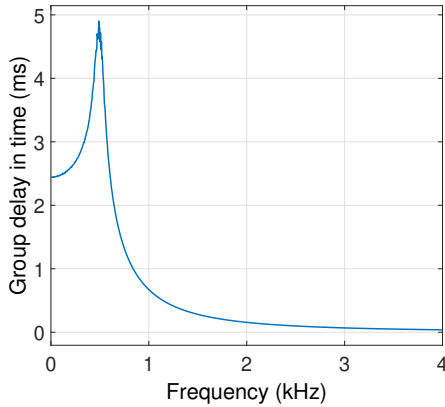
(b) Group delay for the Butterworth filter

Fig. 9. Magnigute and group delay for the Butterworth filter.

B. Peak Detector Scheme

We implement the peak detector, evaluating the slope at the output of the Envelope detector block and comparing it to zero. This low complex mechanism is depicted with the two blocks in Fig. 8. We implement a differentiator with a delay and a subtractor blocks to follow the slope of the envelope. The differentiator's output is compared to zero to produce the synchronization signal with the nanosensor's position. To reduce the variability at the output, the differentiator employs a delay block equivalent to 20 pulse periods, which in turn introduces an additional processing delay of $20 \times T_p = 20\,\mathrm{ms}$. In total, the DSP chain in Fig. 8 introduces a minimum STO of 25 ms.

Fig. 10 illustrate the functioning of the synchronization scheme. The zero crossing results quite close to the minimum communication distance with some STO. The STO is mainly due to the envelope's ripple and the non-zero group delay introduced by the envelope and peak detector blocks. Next Section will discuss the performance of the proposed scheme with noise. We will evaluate the STO with the SNR and the impact on the communication performance with the BER metric.
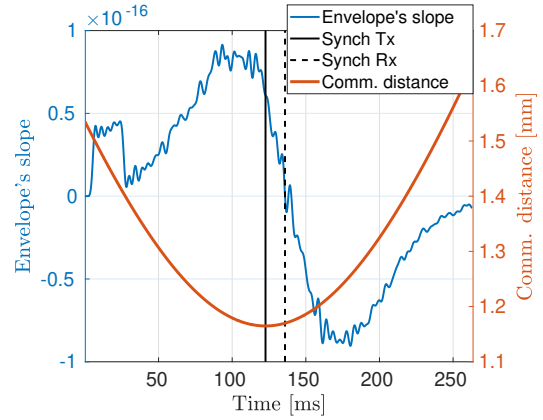

Fig. 10. Recovered synchronization signal.

C. Complexity of the Proposed Synchronization Scheme

The proposed scheme for the synchronizer is comprised mainly of three blocks: the matched filter, the envelope detector, and the peak detector, as depicted in Fig. 8. We evaluate complexity regarding the multipliers and adders needed for each individual block as summarized in Table II. We count the multipliers with the total of coefficients not equal to zero or one. For instance, all the matched filter coefficients are equal to one (as the reference signal is a rectangular pulse of amplitude one, see Fig. 7 a)), thereby its implementation only consists of adders. Furthermore, we used the pulse duration T and sampling time T_s as given in Table I to compute the matched filter total of coefficients, as indicated in Table II.

We remark that the complexity of the proposed scheme increases linearly with the symbol time and similarly with the sampling frequency. As follows from the "Matched Filter" entry in Table II, the total of adders increases linearly with T and with the sampling frequency (f_s), as $T_s = \frac{1}{f_s}$. The hardware implementation for this scheme will require 23 adders and 19 multipliers in total. We also notice that the Butterworth filter is the most complex block to conceive, which can be reduced by implementing a more efficient filter like the elliptic one [36] or decreasing the filter order, we discuss further remarks on this in Section VII.

TABLE II
COMPLEXITY OF THE PROPOSED SYNCHRONIZATION SCHEME.

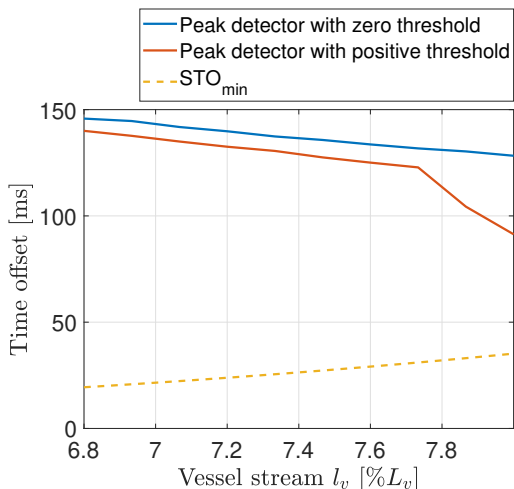| Block	Non-zero coefficients	Adders	Multipliers
Matched Filter	$\frac{T}{T_s} = 5$	4	0
Square block			1
Butterworth Filter	18	18	18
Differentiator	2	1	0
Total		23	19

Fig. 11. Symbol timing offset curves when detecting the peak with the zero interception, and the minimum STO when the noise power is $\sigma^2 = -86.5\,\mathrm{dB}$.
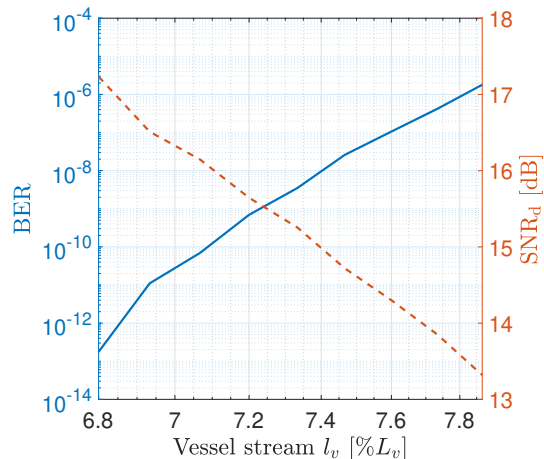

Fig. 12. Comparative BER curves versus SNR for the ideal receiver and the synchronization scheme with zero-crossing detector when the noise power is $\sigma^2 = -86.5\,\mathrm{dB}$.

VI. RESULTS

We evaluate results for the proposed synchronization method illustrating the resulting STO metric and its impact on the BER. We simulate emissions through the channel model introduced in Section III using the reference coordinates in Fig. 2. As for the communication and physiological parameters of the human tissues, we use the values summarized in Table I and in [26, Table I]. Besides, we also evaluate the CRLB as the benchmark for the STO metric.

Fig. 11 illustrates the STO metric with the vessel stream the nanosensor travels, where $l_v \in (0, L_{\mathrm{vessel}})$. We also plot the minimum STO using the CRLB formulation, as given in Section IV-A. For this evaluation, we use the noise level at the input of the peak detector block; see Fig. 8. The resulting noise level is approximately $-86.5\,\mathrm{dB}$ due to the lowpass filter operation, as implemented by the envelope detector block; see Fig. 9.

The STO for the peak detector is in the order of the ms as the case for the minimum STO. Its declining behavior obeys the increased sharpness of the amplitude level with l_v (see Fig. 4 b)), which produces a more abrupt intersection with zero for the slope. Although the STO for the proposed scheme is 5 to 10 times larger than the optimum solution, its impact on the communication performance is quite satisfactory regarding the achievable BER. As depicted in Fig. 12, the BER is less than 1×10^{-5} units and the SNR larger than $13\,\mathrm{dB}$. These results are attainable by the nanosensors traveling at less than $8\,\%$ of the vessel thickness from the vessel wall.

To compute the BER, we assume the simple communication scheme OOK, where the $\mathrm{BER} = Q\left(\sqrt{\mathrm{SNR_d}}\right)$, see [35, Eq. (12) pag. 631].[10] We evaluate for the $\mathrm{SNR_d}$ accounting for the signal-to-noise at the input of the peak detector in Fig. 8, where we evaluate the noise power as $\sigma^2 = -86.5\,\mathrm{dB}$.

The resulting STO for the proposed method is produced by the delay introduced in the processing chain, mainly by two

blocks. On the one hand, by the lowpass filter, and on the other hand, the delay introduced by the differentiator scheme; see Fig. 8. Overcoming this delay, the STO can be further reduced when anticipating the RSS's peak. That can be accomplished when comparing the estimated envelope with a positive value instead of zero.

To illustrate the room for performance improvements, Fig. 11 depicts the resulting STO when increasing the threshold to a positive value; 3×10^{-17} in this case. This threshold value was manually adjusted after visualizing the computed slope (see Fig. 10). Although this positive threshold value is not optimal, it still reduces the STO along the vessel stream compared to the case where the threshold is zero. A real system application will require an adaptive or learning mechanism to anticipate the RSS peak with the vessel stream l_v; in this way compensating for the processing-chain delays.

In contrast to the CRLB formulation, both mechanisms sketch a declining behavior for the STO in the range 6.8 to $8\,\%$ with l_v, as depicted in Fig. 11. This behavior obeys the increased sharpness with l_v for the RSS amplitude, as illustrated in Fig. 4 b). The narrower the peak, the more abrupt the transition with zero, thereby, a more accurate estimate of the symbol arrival. Although this is the case with the proposed method, more accurate solutions will exhibit the same increasing behavior of the CRLB with l_v.

Finally, we also illustrate results in Fig. 13 for the BER metric when using the same positive threshold value. Comparing results with Fig. 12, the SNR increases in around $2\,\mathrm{dB}$. Consequently, the BER decreases significantly by 10^4 units. Such an improvement illustrates the capabilities for fine-tuning the proposed synchronization scheme.

VII. FURTHER RESEARCH DIRECTIONS

During this research, we also identified several open research directions. Aiming to advance the receiver's design further, we elaborate on the following items

- Designing the synchronization scheme with the optimal complexity: According to the discussion in Section V-C,

---

[10]Using this formulation, we implicitly assume there is an ideal clock recovery mechanism; performance degradation is only produced due to transmissions occurring at shifted positions from below the gateway location.
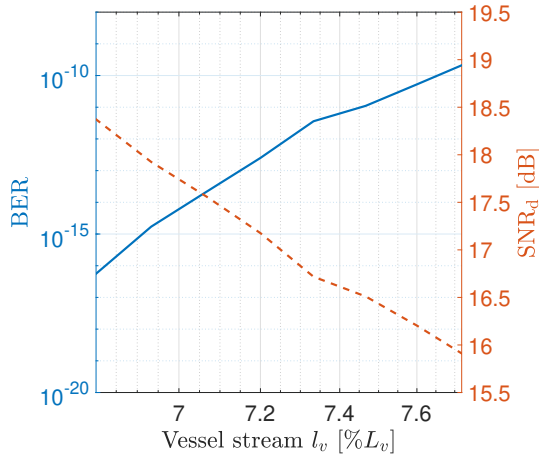
Fig. 13. Comparative BER curves versus SNR for the ideal receiver and the synchronization scheme when using a positive threshold.

the lowpass filter in the Envelope Detector block (see Fig. 8) results in the most complex block to implement due to the number of multipliers and adders needed. This complexity can be reduced at the expense of increased variability for the filter's output signal, which eventually will increase the STO when detecting the envelope's peak. However, the envelope's variability can be reduced by increasing the buffer size for the differentiator block, although it will also increase the STO. For a given STO, it is still pending to minimize the complexity, looking at the balance between the lowpass filter's order and the differentiator block's buffer size.

- Reducing further the STO adapting the threshold value: Aiming to reduce the STO, the received RSS's peak can be anticipated with a positive threshold value; see the discussion in Section VI. This value will depend on the vessel stream the nanosensor is traveling in, which is generally unknown. However, this threshold can be adjusted heuristically by implementing an adaptive mechanism with the slope of the received RSS sequence. For instance, as the slope increases, the threshold can increase to anticipate the RSS's peak, and it can stop increasing with the this slope approaching zero. This way, the estimated RSS's peak can be closer to the actual one.

- Implementing RADAR signal processing solutions to further reduce the STO: Another direction to reduce the STO is looking at RADAR-based solutions like pulse compression techniques. These signal-processing methods narrow the envelope of the received signal after detection, thereby improving the peak location with time. Instead of emitting a sequence of pulses, as illustrated in Fig. 7 b), a frequency-modulated pulse can be emitted to later decode it with reduced time-variability; see, for instance, linear frequency-modulated pulses in [37, Sec. 4.6].

- More realistic models: The antenna beam pattern will also impact the perceived power and the synchronization performance. This work assumes an isotropic antenna; however, in practice, the gateway and nanosensor antennas

implement a radiation pattern with a given communication direction. With the nanosensor's mobility in the blood vessels, the antennas will not always be oriented to each other, thereby preventing a direct communication link with the gateway. A model accounting for the impact of antennas orientation in the synchronization performance will account for more realistic results. Furthermore, with smaller nanosensor sizes, it will also vary its radial position when traveling in the blood; see simulation results in [38]. In such a case, diffusion might dominate advection, causing the received signal strength variability. Such variability will also impact the detection for the RSS's peak, thereby the synchronization performance. A model for the impact of nanosensor's radial mobility in the synchronization performance is missing.

- Synchronization of a cluster of nanosensors with the gateway: When considering a cluster of nanosensors, some of them will travel closer to the gateway, enabling communication, and some others will be limited. In this regard, there is a need to account for models that evaluate the amount of nanosensors that might travel in the communication range of the gateway. It is necessary to model their distribution across the vessel's cross-sectional area and devise communication schemes between the nanosensors at the farthest distance and those closer to the gateway. Recent studies can be used to include realistic transport models for the traveling nanosensors in the capillaries. As indicated in [38], the radial transport in the capillary flow highly depends on the nanosensor size, which will ultimately determine their communication capabilities with the gateway.

VIII. Conclusion

Going well beyond the state of the art, we introduced a low-complex synchronization method enabling terahertz communications via intra-body links. The proposed scheme becomes relevant for interfaces between external gateways and nanosensors operating in the human body. In addition to the conceptual design, we analyzed the communication performance's theoretical bounds. Using a Cramer-Rao lower bound formulation, the minimum achievable symbol timing offset (STO) is in the order of the ms when nanosensors travel in the proximity of the vessel walls and for typical noise power values in the terahertz band. Our findings illustrate the feasibility of such a low-complex synchronization method achieving a BER less than 1×10^{-5} for those nanosensors traveling close to the upper vessel wall. Next research direction is to integrate this synchronization method with a realistic communication scheme, where a clock synchronization method needs to be implemented. In addition, this paper also summarized challenging research directions to advance the receiver's design further and introduce more realistic scenarios.

REFERENCES

[1] D.-H. Kim, N. Lu, R. Ma, Y.-S. Kim, R.-H. Kim, S. Wang, J. Wu, S. M. Won, H. Tao, A. Islam, K. J. Yu, T.-i. Kim, R. Chowdhury, M. Ying, L. Xu, M. Li, H.-J. Chung, H. Keum, M. McCormick, P. Liu, Y.-W. Zhang, F. G. Omenetto, Y. Huang, T. Coleman, and J. A. Rogers, "Epidermal Electronics," *Science*, vol. 333, no. 6044, pp. 838–843, Aug. 2011.

[2] X. T. Zheng, Z. Yang, L. Sutarlie, M. Thangaveloo, Y. Yu, N. A. B. M. Salleh, J. S. Chin, Z. Xiong, D. L. Becker, X. J. Loh, B. C. K. Tee, and X. Su, "Battery-free and AI-enabled multiplexed sensor patches for wound monitoring," *Science Advances*, vol. 9, no. 24, Jun. 2023.

[3] Y. Yu, J. Nassar, C. Xu, J. Min, Y. Yang, A. Dai, R. Doshi, A. Huang, Y. Song, R. Gehlhar, A. D. Ames, and W. Gao, "Biofuel-powered soft electronic skin with multiplexed and wireless sensing for human-machine interfaces," *Science Robotics*, vol. 5, no. 41, Apr. 2020.

[4] J. M. Jornet and I. F. Akyildiz, "Femtosecond-Long Pulse-Based Modulation for Terahertz Band Communication in Nanonetworks," *IEEE Transactions on Communications*, vol. 62, no. 5, pp. 1742–1754, May 2014.

[5] P. K. B. Rangaiah, R. L. Karlsson, A. S. Chezhian, L. Joseph, B. Mandal, B. Augustine, M. Mani, M. D. Perez, T. Voigt, and R. Augustine, "Realization of a Portable Semi-Shielded Chamber for Evaluation of Fat-Intrabody Communication," *IEEE Access*, vol. 11, pp. 72 743–72 755, 2023.

[6] I. F. Akyildiz, M. Ghovanloo, U. Guler, T. Ozkaya-Ahmadov, A. F. Sarioglu, and B. D. Unluturk, "PANACEA: An Internet of Bio-NanoThings Application for Early Detection and Mitigation of Infectious Diseases," *IEEE Access*, vol. 8, pp. 140 512–140 523, Jan. 2020.

[7] F. Dressler and S. Fischer, "Connecting In-Body Nano Communication with Body Area Networks: Challenges and Opportunities of the Internet of Nano Things," *Elsevier Nano Communication Networks*, vol. 6, pp. 29–38, Jun. 2015.

[8] J. Torres Gómez, J. Angjo, and F. Dressler, "Age of Information-based Performance of Ultrasonic Communication Channels for Nanosensor-to-Gateway Communication," *IEEE Transactions on Molecular, Biological and Multi-Scale Communications*, vol. 9, no. 2, pp. 112–123, Jun. 2023.

[9] J. M. Jornet and A. Sangwan, "Nanonetworking in the Terahertz Band and Beyond," *IEEE Nanotechnology Magazine*, vol. 17, no. 3, pp. 21–31, Jun. 2023.

[10] A. Sangwan and J. M. Jornet, "Joint Communication and Bio-Sensing With Plasmonic Nano-Systems to Prevent the Spread of Infectious Diseases in the Internet of Nano-Bio Things," *IEEE Journal on Selected Areas in Communications*, vol. 40, no. 11, pp. 3271–3284, Nov. 2022.

[11] A. Abohmra, F. Jilani, H. T. Abbas, A. Alomainy, M. Ur-Rehman, M. A. Imran, and Q. H. Abbasi, "Flexible and Wearable Graphene-based Terahertz Antenna for Body-Centric Applications," in *International Workshop on Mobile Terahertz Systems (IWMTS 2019)*, Bad Neuenahr-Ahrweiler, Germany: IEEE, Jul. 2019.

[12] F. Lemic, S. Abadal, W. Tavernier, P. Stroobant, D. Colle, E. Alarcon, J. M. Marquez-Barja, and J. Famaey, "Survey on Terahertz Nanocommunication and Networking: A Top-Down Perspective," *IEEE Journal on Selected Areas in Communications*, vol. 39, no. 6, pp. 1506–1543, Jun. 2021.

[13] J. M. Jornet and I. F. Akyildiz, "Channel Modeling and Capacity Analysis for Electromagnetic Wireless Nanonetworks in the Terahertz Band," *IEEE Transactions on Wireless Communications*, vol. 10, no. 10, pp. 3211–3221, Oct. 2011.

[14] S. Tarboush, H. Sarieddeen, M.-S. Alouini, and T. Y. Al-Naffouri, "Single- Versus Multicarrier Terahertz-Band Communications: A Comparative Study," *IEEE Open Journal of the Communications Society*, vol. 3, pp. 1466–1486, 2022.

[15] P. Singh and S.-Y. Jung, "Multilevel Pulse Position Modulation With Level Trimming for Electromagnetic Nanocommunications in the Terahertz Band," *IEEE Access*, vol. 10, pp. 94 158–94 168, 2022.

[16] I. F. Akyildiz, C. Han, Z. Hu, S. Nie, and J. M. Jornet, "Terahertz Band Communication: An Old Problem Revisited and Research Directions for the Next Decade," *IEEE Transactions on Communications*, vol. 70, no. 6, pp. 4250–4285, Jun. 2022.

[17] A. Gupta, M. Medley, and J. M. Jornet, "Joint Synchronization and Symbol Detection Design for Pulse-Based Communications in the THz Band," in *IEEE Global Communications Conference (GLOBECOM 2015)*, San Diego, CA: IEEE, Dec. 2015.

[18] R. G. Cid-Fuentes, J. M. Jornet, I. F. Akyildiz, and E. Alarcon, "A receiver architecture for pulse-based electromagnetic nanonetworks in the Terahertz Band," in *IEEE International Conference on Communications (ICC 2012)*, Ottawa, Canada: IEEE, Jun. 2012.

[19] C. Han, I. F. Akyildiz, and W. H. Gerstacker, "Timing Acquisition and Error Analysis for Pulse-Based Terahertz Band Wireless Systems," *IEEE Transactions on Vehicular Technology*, vol. 66, no. 11, pp. 10 102–10 113, Nov. 2017.

[20] J. Torres Gómez, J. Simonjan, J. M. Jornet, and F. Dressler, "Optimizing Terahertz Communication Between Nanosensors in the Human Cardiovascular System and External Gateways," *IEEE Communications Letters*, vol. 27, no. 9, pp. 2318–2322, Sep. 2023.

[21] Q. Xia, Z. Hossain, M. Medley, and J. M. Jornet, "A Link-Layer Synchronization and Medium Access Control Protocol for Terahertz-Band Communication Networks," *IEEE Transactions on Mobile Computing*, vol. 20, no. 1, pp. 2–18, Jan. 2021.

[22] N. Saeed, M. H. Loukil, H. Sarieddeen, T. Y. Al-Naffouri, and M. S. Alouini, "Body-Centric Terahertz Networks: Prospects and Challenges," *IEEE Transactions on Molecular, Biological and Multi-Scale Communications*, vol. 8, no. 3, pp. 138–157, Sep. 2022.

[23] H. Chen, H. Sarieddeen, T. Ballal, H. Wymeersch, M.-S. Alouini, and T. Y. Al-Naffouri, "A Tutorial on Terahertz-Band Localization for 6G Communication Systems," *IEEE Communications Surveys & Tutorials*, vol. 24, no. 3, pp. 1780–1815, 2022.

[24] H. C. Berg, *Random Walks in Biology*. Princeton University Press, 1993.

[25] V. Jamali, A. Ahmadzadeh, W. Wicke, A. Noel, and R. Schober, "Channel Modeling for Diffusive Molecular Communication - A Tutorial Review," *Proceedings of the IEEE*, vol. 107, no. 7, pp. 1256–1301, Jul. 2019.

[26] J. Simonjan, B. D. Unluturk, and I. F. Akyildiz, "In-body Bionanosensor Localization for Anomaly Detection via Inertial Positioning and THz Backscattering Communication," *IEEE Transactions on NanoBioscience*, vol. 21, no. 2, pp. 216–225, Apr. 2022.

[27] G. Piro, P. Bia, G. Boggia, D. Caratelli, L. A. Grieco, and L. Mescia, "Terahertz electromagnetic field propagation in human tissues: A study on communication capabilities," *Nano Communication Networks*, vol. 10, pp. 51–59, Dec. 2016.

[28] P. Oltulu, B. Ince, N. Kokbudak, S. Findik, and F. Kilinc, "Measurement of epidermis, dermis, and total skin thicknesses from six different body regions with a new ethical histometric technique," *Turkish Journal of Plastic Surgery*, vol. 26, no. 2, p. 56, 2018.

[29] M. Fruchard, L. Arcese, and E. Courtial, "Estimation of the Blood Velocity for Nanorobotics," *IEEE Transactions on Robotics and Automation*, vol. 30, no. 1, pp. 93–102, Feb. 2014.

[30] A. Rogalski, "Graphene-based materials in the infrared and terahertz detector families: a tutorial," *Advances in Optics and Photonics*, vol. 11, no. 2, p. 314, May 2019.

[31] A. C. Guyton and M. E. Hall, *Guyton and Hall Textbook of Medical Physiology*, 14th ed. Elsevier, 2015.

[32] M. S. Chaudhari and S. Majhi, "STO Estimation for OFDM System Using CDM," *IEEE Communications Letters*, vol. 26, no. 11, pp. 2651–2655, Nov. 2022.

[33] S. Kay, *Fundamentals of Statistical Signal Processing: Estimation Theory*. Upper Saddle River, NJ: Prentice Hall, 1998.

[34] B. Sklar, *Digital Communications: Fundamentals and Applications*, 2nd ed. Upper Saddle River, NJ: Prentice Hall, 2001.

[35] A. B. Carlson, P. B. Crilly, and J. C. Rutledge, *Communication Systems: An Introduction to Signals and Noise in Electrical Communication*, 4th ed. New York City, NY: McGraw-Hill, 2002, p. 850.

[36] A. V. Oppenheim and R. W. Schafer, *Discrete-time signal processing*, 3rd ed. Upper Saddle River, NJ: Prentice Hall, 2010.

[37] M. A. Richards, *Fundamentals of Radar Signal Processing*, 2nd ed. New York City, NY: McGraw-Hill Education, 2014, p. 894.

[38] T.-R. Lee, M. Choi, A. M. Kopacz, S.-H. Yun, W. K. Liu, and P. Decuzzi, "On the near-wall accumulation of injectable particles in the microcirculation: smaller is not better," *Scientific Reports (Sci. Rep.)*, vol. 3, no. 1, Jun. 2013.

Jorge Torres Gómez received the B.Sc., M.Sc., and Ph.D. degrees from the Technological University of Havana, CUJAE, Cuba, in 2008, 2010, and 2015, respectively. He is currently with the Telecommunication Networks Group, Department of Telecommunication Systems, Technical University of Berlin. He holds a position as head of educational activities at the IEEE Germany Section, supporting teaching activities and chairing conference events in education. Since 2008, he has been with the School of Telecommunications and Electronics, CUJAE University, where he was a Lecturer from 2008 to 2018. He has been with the Department of Signal Theory and Communications, Carlos III University of Madrid, Leganés Campus, Madrid, Spain, as a guest lecturer, and with the Department of Digital Signal Processing and Circuit Technology, Chemnitz University of Technology as a postdoc. His research interests include molecular communications, nanonetworks, the age of information, and digital signal processing.

Jennifer Simonjan received her Ph.D. degree in Information and Communication Engineering from the University of Klagenfurt, Austria in 2019. After her Ph.D, she gathered experience working as a post doc at the Georgia Institute of Technology in Atlanta, US and as a researcher in Austria. Currently, she works as a lead researcher in the Autonomous Robotics Research Center at the Technology Innovation Institute in Abu Dhabi, UAE. Her research interest comprise self-organization and communication in nanoscale and macroscale sensor networks as well as robotic networks.

Falko Dressler is full professor and Chair for Data Communications and Networking at the School of Electrical Engineering and Computer Science, TU Berlin. He received his M.Sc. and Ph.D. degrees from the Dept. of Computer Science, University of Erlangen in 1998 and 2003, respectively. Dr. Dressler has been associate editor-in-chief for IEEE Trans. on Mobile Computing and Elsevier Computer Communications as well as an editor for journals such as IEEE/ACM Trans. on Networking, IEEE Trans. on Network Science and Engineering, Elsevier Ad Hoc Networks, and Elsevier Nano Communication Networks. He has been chairing conferences such as IEEE INFOCOM, ACM MobiSys, ACM MobiHoc, IEEE VNC, IEEE GLOBECOM. He authored the textbooks Self-Organization in Sensor and Actor Networks published by Wiley & Sons and Vehicular Networking published by Cambridge University Press. He has been an IEEE Distinguished Lecturer as well as an ACM Distinguished Speaker. Dr. Dressler is an IEEE Fellow as well as an ACM Distinguished Member. He is a member of the German National Academy of Science and Engineering (acatech). He has been serving on the IEEE COMSOC Conference Council and the ACM SIGMOBILE Executive Committee. His research objectives include adaptive wireless networking (sub-6GHz, mmWave, visible light, molecular communication) and wireless-based sensing with applications in ad hoc and sensor networks, the Internet of Things, and Cyber-Physical Systems.